SCIENTIFIC REPORTS
nature research

OPEN

Sugar alcohol provides imaging contrast in cancer detection

Puneet Bagga[1], Neil Wilson[1], Laurie Rich[1], Francesco M. Marincola[2], Mitchell D. Schnall[1], Hari Hariharan[1], Mohammad Haris[1,2,3] & Ravinder Reddy[1]

Received: 10 January 2017
Accepted: 9 July 2019
Published online: 31 July 2019

Clinical imaging is widely used to detect, characterize and stage cancers in addition to monitoring the therapeutic progress. Magnetic resonance imaging (MRI) aided by contrast agents utilizes the differential relaxivity property of water to distinguish between tumorous and normal tissue. Here, we describe an MRI contrast method for the detection of cancer using a sugar alcohol, maltitol, a common low caloric sugar substitute that exploits the chemical exchange saturation transfer (CEST) property of the labile hydroxyl group protons on maltitol (malCEST). *In vitro* studies pointed toward concentration and pH-dependent CEST effect peaking at 1 ppm downfield to the water resonance. Studies with control rats showed that intravenously injected maltitol does not cross the intact blood-brain barrier (BBB). In glioma carrying rats, administration of maltitol resulted in the elevation of CEST contrast in the tumor region only owing to permeable BBB. These preliminary results show that this method may lead to the development of maltitol and other sugar alcohol derivatives as MRI contrast agents for a variety of preclinical imaging applications.

Medical imaging is widely used to monitor structural, functional, and molecular changes in cancer and the use of contrast agents has significantly improved the detection by providing enhanced contrast between normal and pathological tissues[1–4]. Positron Emission Tomography using ^{18}Fluoro-2-deoxy-glucose (^{18}FDG-PET) combined with either computed tomography (CT) or magnetic resonance imaging (MRI) has gained widespread application as a molecular and metabolic imaging modality of cancers based on the high glycolytic activity of tumors[5,6]. However, owing to the high metabolic activity of surrounding neurons, ^{18}F-FDG uptake in the normal brain tissue limits its use for the imaging of cerebral gliomas[7]. In addition to conventional MRI, dynamic contrast enhanced (DCE) MRI utilizes the relaxivity perturbation potential of gadolinium-based contrast agents (GBCAs) to detect and characterize cancer[8]. Although, recent studies have reported the deposition of GBCAs in the brain and bone matrix[3,9,10], further studies are required to evaluate the long-term effects of gadolinium (Gd) accumulation on normal tissue function.

The Chemical Exchange Saturation Transfer (CEST) MRI technique probes the exchange of labile protons of the solute with bulk water protons[11–15]. By applying low-power frequency-selective radio-frequency (RF) pulses for a long time, magnetization of exchangeable protons on a metabolite can be saturated. The chemical exchange mediated accumulation of these saturated protons with water decreases the bulk water signal in a concentration and pH dependent manner[14,16,17]. The difference in the water signal obtained with and without RF saturation can be measured as the CEST contrast[14,15]. CEST MRI has been used to image different metabolites and macromolecules *in vivo*, with applications in several human disorders[18–23]. Since the CEST method provides orders of magnitude higher sensitivity than traditional proton MR spectroscopy (^{1}H MRS), it enables detection of subtle changes in the level of metabolite of interest[14,17]. Various groups have reported the use of glucose and its analogues as CEST contrast agent to study cancer and neurodegeneration[18,20,24–34].

In this study, we introduce a new contrast agent, maltitol, a sugar alcohol commonly used as a sweetener due to its less caloric value. We exploited the CEST behavior of labile hydroxyl (-OH) protons on maltitol with those of the bulk water and termed this new method as malCEST. The concentration and pH dependence of malCEST contrast was measured *in vitro* in solution phantoms. The potential of malCEST as an MR imaging method to image cancer was assessed in a rat glioma model and compared with gadolinium-diethylenetriamine-pentaacetic-acid (Gd-DTPA) contrast enhanced MRI.

[1]Center for Magnetic Resonance and Optical Imaging, Department of Radiology, University of Pennsylvania, Philadelphia, PA, USA. [2]Research Branch, Sidra Medical and Research Center, Doha, Qatar. [3]Laboratory Animal Research Center, Qatar University, Doha, Qatar. Correspondence and requests for materials should be addressed to R.R. (email: krr@pennmedicine.upenn.edu)

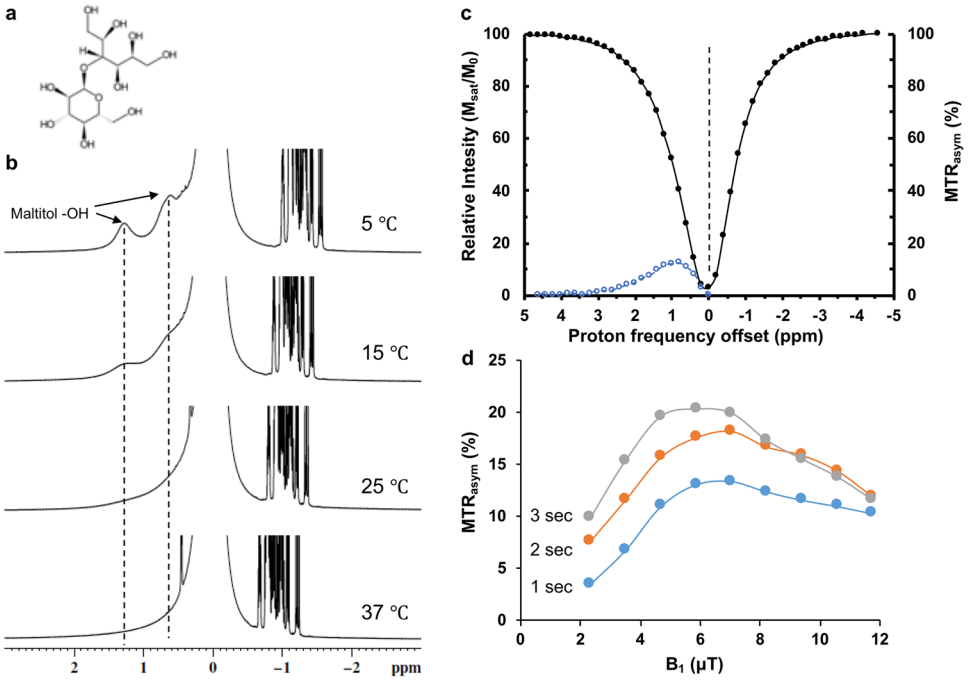

Figure 1. CEST effect from maltitol sweetener. (**a**) Chemical structure of maltitol. (**b**) High resolution NMR spectrum of 200 mM maltitol solution in PBS shows two peaks from exchangeable hydroxyl protons (-OH) respectively at 0.8 and 1.3 ppm at 5 °C. These peaks exchange broaden with increase in temperature and completely broadened at 37 °C. (**c**) Z-spectra (black) and asymmetry curves (blue) from 10 mM of maltitol show broad resonance (0–3 ppm) from exchangeable hydroxyl protons, which peaks at 1 ppm. (**d**) Saturation power and saturation dependence malCEST contrast. Higher B_1 and saturation duration increase the malCEST effect.

Results

Chemical evaluation of exchangeable protons of maltitol. Maltitol is a disaccharide of glucose and sorbitol, having 9 water exchangeable -OH groups (Fig. 1a). Chemical shift of the labile -OH protons of maltitol was determined using high-resolution nuclear magnetic resonance (NMR) spectroscopy. The spectra from 200 mM maltitol (pH 7) were acquired at different temperatures (5, 15, 25, & 37 °C) on a 400 MHz NMR spectrometer (Bruker, Germany). Two peaks at ~0.8 and ~1.3 ppm down field of water were detected due to slower exchange between maltitol -OH protons and bulk water at low temperatures (Fig. 1b). The -OH peaks were found to broaden at higher temperatures due to faster chemical exchange and completely disappear at 37 °C. The observation of -OH peaks at ~1 ppm downfield to water signal suggests the feasibility of CEST based experiments using maltitol.

Evaluation of CEST effect from maltitol. The characterization of CEST effect from maltitol was performed by applying a continuous low power saturating RF pulses at frequencies gradually moving away from the reference water peak are visualized by plotting the water saturation as a function of saturation frequency. The z-spectra and z-spectral asymmetry (MTR_{asym}) curves obtained from maltitol solution showed maximal malCEST effect at 1 ppm (Fig. 1c). The malCEST contrast from 10 mM maltitol solution *in vitro* was found to be maximum at ~6 μT saturation power (B_1) for all saturation durations (Fig. 1d). For a given B_1, higher malCEST contrast was observed with the increase in saturation duration (Fig. 1d).

Concentration and pH dependence of malCEST contrast. The concentration dependence of malCEST contrast was evaluated *in vitro* on solution phantoms prepared at physiological pH and temperature (37 °C). The $MTR_{asym@1ppm}$ map from 10 mM phantom showed ~13% of malCEST contrast (Fig. 2a) and was linearly proportional to the maltitol concentration with a slope of 1.3% per mM of maltitol (Fig. 2b). The malCEST effect was found to be inversely proportional to pH (Fig. 2c,d). The data acquired from maltitol solution at varying pH depicted 14.8% increase in malCEST per unit decrease in pH. The malCEST map from 10 mM maltitol solution acquired on 7 T human MRI scanner is shown in the Supplementary Fig. 1.

CEST MRI experiments in control rats. To assess whether maltitol crosses the intact BBB, an *in vivo* study was performed on control rats (n = 3). At the given saturation parameters (2.35 μT, 2 sec), a baseline 2–3% $MTR_{asym@1ppm}$ was observed. This may be due to the endogenous metabolites with -OH groups present in the brain predominantly myo-inositol and glucose. The malCEST contrast maps from a normal rat brain were acquired at different time intervals over a period of 70 minutes during and following the intravenous injection of maltitol (Fig. 3a). No appreciable change in the malCEST contrast was observed in the normal rat brain over the period of 70 minutes (Fig. 3b) most likely due to the intact blood-brain barrier (BBB).

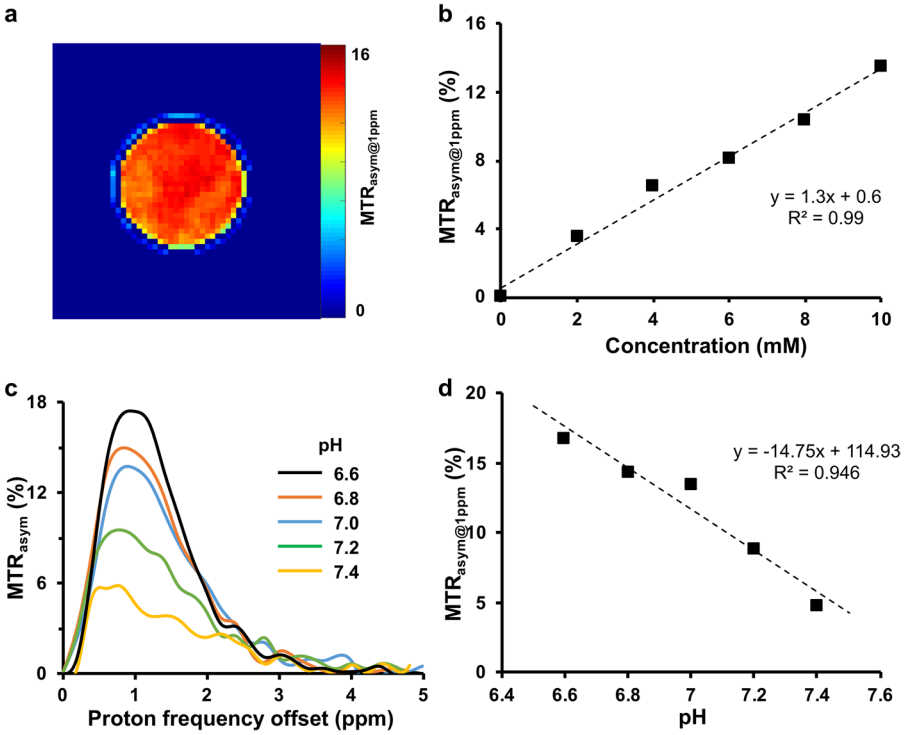

Figure 2. MalCEST map of maltitol. (**a**) malCEST map obtained from 10 mM maltitol solution phantom at 37 °C shows homogenous contrast. (**b**) Plot depicts the concentration dependent malCEST contrast. (**c**) Z-spectra asymmetry curves at different pH show higher malCEST contrast with decrease in pH. (**d**) inverse linear correlation between malCEST and pH was observed.

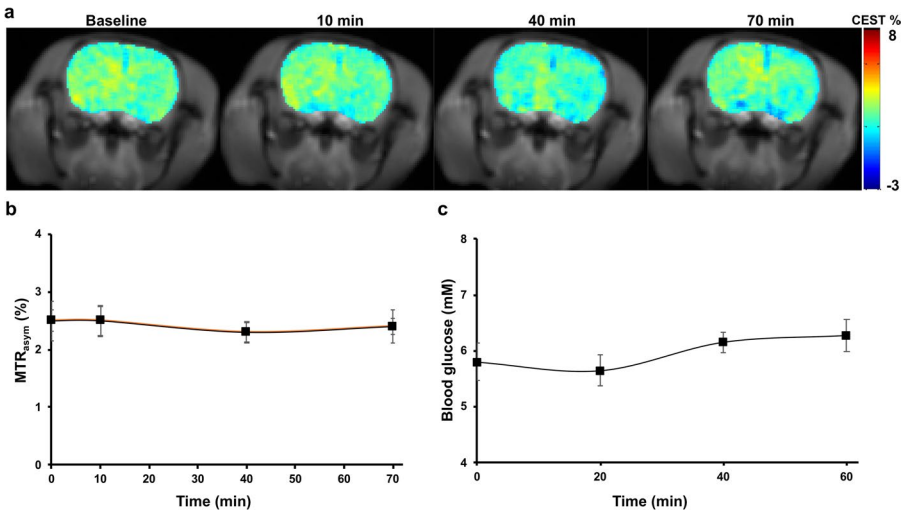

Figure 3. MalCEST imaging in a normal rat brain. (**a**) CEST MRI from a normal rat brain depicts no appreciable change in the malCEST contrast following injection of maltitol over 70 min. (**b**) Data from the normal rats (n = 3) shows no change in malCEST contrast in the brain during and following maltitol administration. (**c**) There was no observable change in the blood glucose levels post maltitol administration.

To evaluate the effect of intravenously injected maltitol on the blood glucose level, 50 µl of blood was collected every 20-minute time interval for up to period of 60 minutes. The blood glucose level during period of 60 minutes following the beginning of maltitol infusion was found to remain the same (Fig. 3c), indicating that there was no hydrolysis of maltitol into glucose and sorbitol. Further, the blood pH following maltitol administration was found to be unaltered until 60 minutes in three control rats.

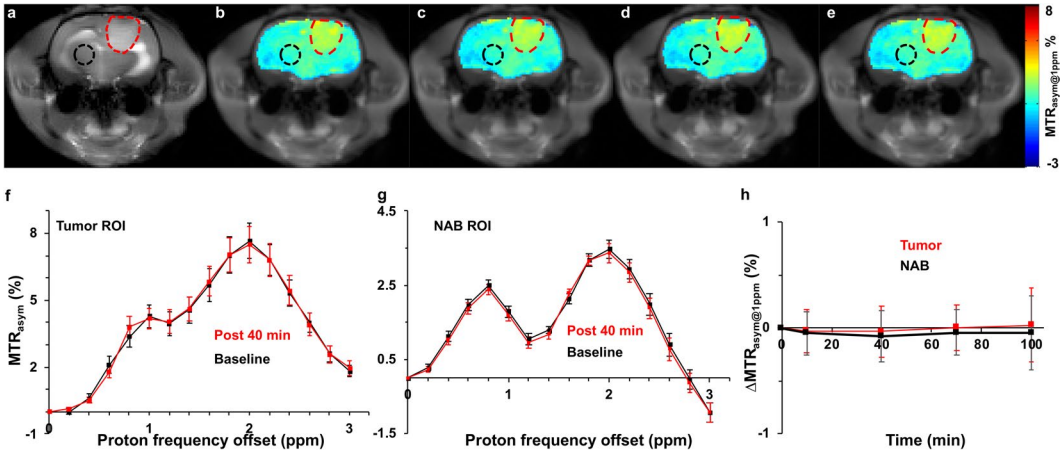

Figure 4. Normal saline perfused malCEST imaging in glioma. (**a**) Anatomical proton weighted image shows tumor as a hyperintense region. (**b**–**e**) $MTR_{asym@1ppm}$ maps at different time points show no appreciable change in the CEST contrast at 1 ppm from tumor (red outline) and normal appearing brain (black outline) regions following administration of normal saline (**b** Pre-injection; **c**, 10 min; **d**, 40 min and **e**, 70 min post the beginning of normal saline administration). (**f**) MTR asymmetry curves from ROIs placed in the tumor region generated at baseline and 40 minutes post infusion of normal saline showing unaltered MTR_{asym}. (**g**) Asymmetry curves from ROIs placed in the NAB region generated Pre- and Post 40 minutes showing no change in MTR_{asym} from normal saline. (**h**) $\Delta MTR_{asym@1ppm}$ ($MTR_{asym@1ppm}Post - MTR_{asym@1ppm}Pre$) contrast was unaltered during and following normal saline administration in both tumor and NAB ROIs.

CEST experiments on glioma rats. To assess the potential of maltitol for providing CEST contrast to image cancer *in vivo*, we performed MR imaging experiments on rats carrying 9 L glioma. As the maltitol solution for MRI experiments was prepared in normal saline (NS), it is necessary to determine the effect of NS on the CEST contrast post intravenous administration. The MTR_{asym} maps at 1 ppm shown in Fig. 4 demonstrate no change in the CEST contrast pre and post-NS administration indicating NS does not contribute to the CEST changes in further experiments. Following this, we performed MR studies including T1/T2-weighted and CEST MRI in glioma carrying rats ($n = 5$) by administrating maltitol. The T2 weighted image showed hyperintensity in the tumor (Fig. 5a), correspondingly, Gd-DTPA enhanced T1-weighted image clearly highlighted the tumor region (Fig. 5b). The malCEST contrast measured post administration of maltitol highlighted only the tumor region (Fig. 5c–g) presumably due to the accumulation of maltitol in the extracellular and extravascular space (EES) because of the enhanced BBB permeability and retention effect. The MTR_{asym} curves obtained pre- and post-maltitol administration clearly showed increase in the CEST contrast at 1 ppm demonstrating that the change is due to EES accumulation of maltitol in the tumor (Pre: $2.33 \pm 0.24\%$, Post 40 min: $3.95 \pm 0.44\%$; $p < 0.001$) (Fig. 6a,b). There was no appreciable change in the malCEST contrast in the normal appearing brain regions (Pre: $1.62 \pm 0.10\%$, Post 40 min: $1.69 \pm 0.15\%$; $p = 0.84$) (Fig. 6c), which further confirms that maltitol does not cross the intact BBB. In the tumor, malCEST contrast peaked at ~40 minutes during the intravenous administration (Fig. 6d). The change in the malCEST contrast between tumor and contralateral normal appearing brain (NAB) ROIs post 40 minutes from the beginning of maltitol infusion was found to be statistically significant (Tumor: $1.62 \pm 0.10\%$, NAB: $0.07 \pm 0.02\%$; $p < 0.001$).

Discussion

In this study, we showed the potential of a commonly used low calorific sweetener, maltitol, as an MRI contrast agent in imaging cancer by exploiting the exchange-based property of maltitol hydroxyl protons with those of bulk water. The chemical shift of the exchangeable hydroxyl protons of maltitol was found to be between 0.7–1.4 ppm downfield of water allowing its application as a possible CEST contrast agent. Being a small molecule, maltitol can easily accumulate in the cancerous tissues. Moreover, maltitol does not have a metabolic fate in the tumor due to the absence maltase enzyme responsible for the breakdown of maltitol into glucose and sorbitol.

D-glucose and its analogues have shown potential as CEST contrast agents for the non-invasive detection of various cancers in preclinical and clinical studies[18,28–31,33,35–40]. Dynamic glucose-enhanced (glucoCEST) MRI has been used to study perfusion in cancer which corroborated with DCE MRI utilizing GBCAs. Recently, glucoCEST has been used to evaluate the efficacy of rapamycin, a glucose transporter blocker, in preclinical model of glioblastoma[20]. This study reported a higher glucoCEST contrast from tumor post-treatment with rapamycin. In addition, non-metabolized glucose analogues such as 3-O-methylglucose (3-OMG), have been exploited as CEST contrast agents for studies in cancer and stroke[24–26,28–30,32]. Further, another study has shown the use of a non-caloric sweetener, sucralose, as a CEST contrast agent to detect glioma in a preclinical model[41]. There are several other studies involving another glucose analogue, 2-deoxy-D-glucose (2DG) as CEST agent to image cerebral glucose uptake[27] in cancer[35] and Alzheimer's Disease[42].

In the normal brain, the malCEST contrast was unaltered following intravenous injection of maltitol suggesting that maltitol is unable to cross the BBB. However, in the brain tumor model with compromised BBB,

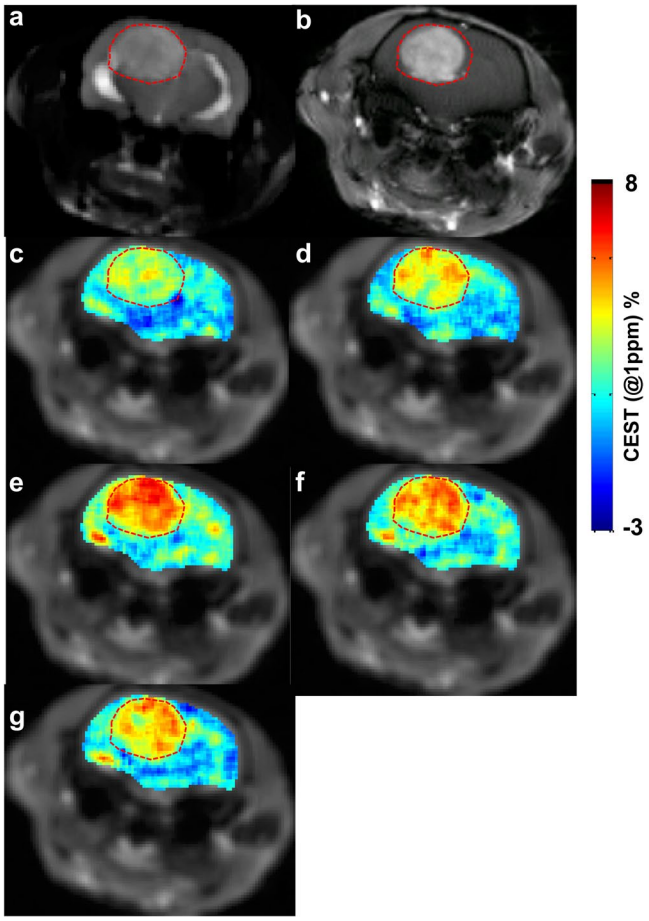

Figure 5. The malCEST map of a rat brain tumor. (**a**) Anatomical T2-weighted image from axial slice showing the location of tumor as hyper intense region in the rat brain. (**b**) The T1-weighted image post Gd-DTPA administration highlights the tumor areas in the brain. (**c**–**g**) malCEST map from rat brain tumor shows increased contrast in tumor region following intravenous injection of maltitol peaking at 40 minutes following the start of injection (**c**, Pre-injection; **d**, 10 min; **e**, 40 min; **f**, 70 min; and **g**, 100 minutes post the beginning of maltitol administration).

the injected maltitol diffuses in the tumor EES and highlights the tumor areas. Significantly higher contrast was observed in the tumorous region at 40 minutes during maltitol infusion, while no change in the normal appearing brain region was observed. The spatial extent of malCEST enhancement appeared to broadly agree with that of the Gd-DTPA enhancement. The current study demonstrates the potential of an alternative high-resolution MR method to image cancers in preclinical models. The kinetics of malCEST contrast may be further evaluated in different cancer types and could potentially be used as a biomarker to differentiate cancer phenotypes.

Maltitol is FDA approved to be consumed orally at very high daily dose up to several grams. The toxicity profile of maltitol has been evaluated in human volunteers following varying oral dose administration, observed no maltitol related adverse effects except at higher doses (70 g/day) where 15–30% volunteers reported diarrhea[43]. Previous studies have shown no toxic effect of intravenously injected maltitol at a dose of ~1.25 g/kg in rats[44]. In the current study, we have used maltitol at a dose of 2.5 g/kg without any observable toxic effects. Since maltitol is not approved by the FDA for intravenous injection in humans, it may be a limiting factor for the clinical translation of this technique. We observed no noticeable side-effects in the rats at the dosage level used in this study. Further, consistent with a previous study, we observed no change in the blood glucose level post maltitol administration[44]. Oral vs intravenous administration has different fates of maltitol inside the body. Oral administration of maltitol has been shown to not increase the blood maltitol level due to its conversion into glucose and sorbitol by the action of maltase present in the gut[45]. Absence of maltase in the rest of the body may be the reason for the observed unaltered blood glucose levels after intravenous injection of maltitol.

Maltitol is reported to have very high clearance rate from the body as reported previously[44]. By 60 minutes following intravenous administration, maltitol is nearly cleared from the blood stream. This may be a reason for the lower retention of the maltitol in the EES resulting in lower observed changes in the $MTR_{assym@1ppm}$. Also, it has been shown that intravenous injected maltitol is virtually cleared from the blood within an hour[44]. Further studies at different doses are needed to validate that the observed CEST contrast arises from maltitol accumulation in the tumor.

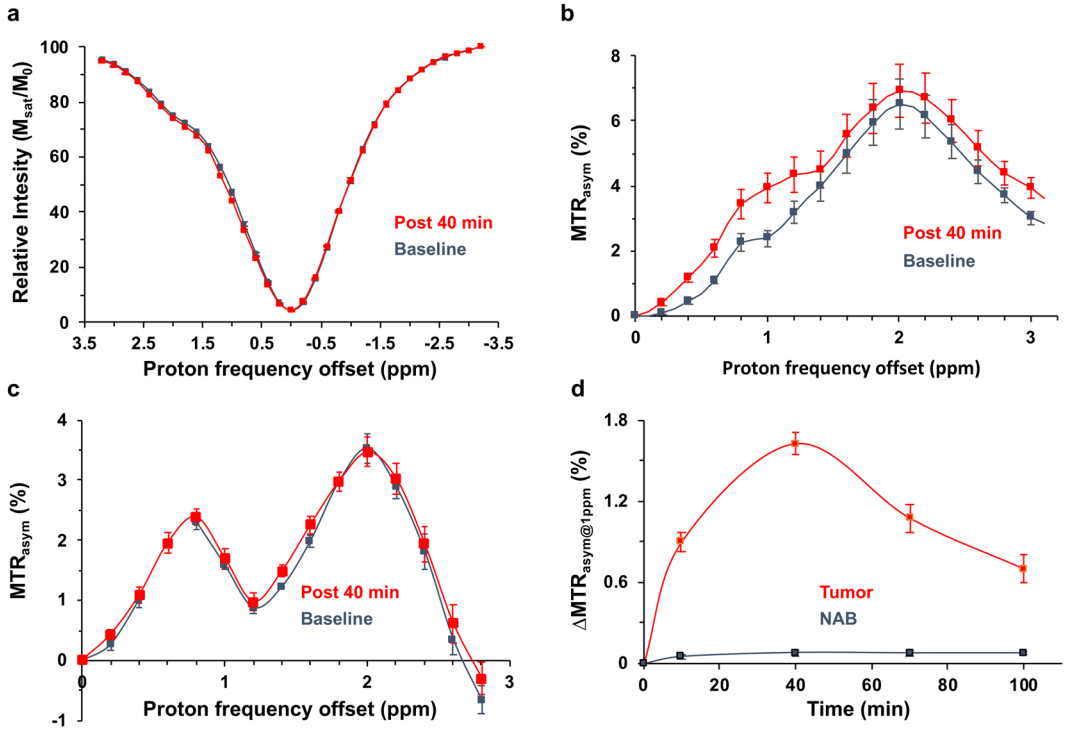

Figure 6. Z-spectra and MTR_{asym} analysis of tumor and normal appearing brain following maltitol administration. (**a**,**b**) Z-spectra and MTR asymmetry curves from ROIs placed in the tumor region generated at baseline and 40 minutes post infusion of maltitol show increased MTR_{asym} at 1 ppm ($MTR_{asym@1ppm}$). (**c**) MTR_{asym} curves from ROIs placed in the normal appearing brain (NAB) region generated at baseline and post 40 minutes showing no change in MTR_{asym} due to intact BBB. (**d**) $\Delta MTR_{asym@1ppm}$ ($MTR_{asym@1ppm}$Post − $MTR_{asym@1ppm}$Pre) contrast at different time points peaks at 40 minutes in the tumor ROI while NAB was unaltered during and following maltitol administration.

Though we have evaluated the concentration and pH dependence of the CEST effect from maltitol *in vitro*, this study lacks data on the differential dosing of malitol on the malCEST contrast *in vivo*. Further studies are required in tumor-bearing animals to optimize the dose for contrast enhancement from the EES accumulation of maltitol. Moreover, though the malCEST enhancement in glioma corroborated with the Gd-DTPA enhanced map, a direct comparison between the two techniques is beyond the scope of this study. It is noteworthy that CEST acquisition times are longer compared to GBCA based DCE MRI studies. Also, CEST MRI in the current study is limited to 2D acquisition of a thick slice to obtain sufficient signal-to-noise ratio, while the GBCA based studies can be performed at significantly higher in-plane resolution and 3D. Finally, the B_1 power and duration optimization performed *in vitro* yielded higher optimal B_1 (~6 μT) for observing malCEST, while a lower B_1 (2.35 μT) was used for *in vivo* experiments. This was due to the reason that high saturation powers cause off-resonance saturation of water leading to the reduction in CEST amplitude, especially when the exchanging protons have a small chemical shift and slow chemical exchange rate[46–49]. Although, maltitol hydroxyl group exchange rate *in vitro* appears to be high, as the extracellular pH (pHe) in tumor tissue is lower than the normal tissue[50], this would lead to a reduction in the exchange rate of the accumulated maltitol hydroxyl groups *in vivo*. Moreover, higher B_1 power results lower SNR *in vivo* than *in vitro* as the water concentration is higher *in vitro* than *in vivo* (~70%)[51].

In conclusion, this preliminary study paves the way for the development of maltitol and other maltitol derivatives as MRI contrast agents to detect cancer and monitor therapeutic response in preclinical studies.

Materials and Methods

Phantom preparation. All the solution phantoms were prepared in phosphate buffered saline (PBS) and the experiments were performed at 37 °C. For high-resolution ^{1}H NMR spectroscopy, 200 mM of maltitol (Sigma Aldrich, USA) solution was prepared in PBS at pH 7. To measure the pH dependence of malCEST, phantoms with 10 mM maltitol concentration in PBS were prepared at a varying pH from 6.6 to 7.4 in step of 0.2 pH unit. The pH was adjusted using 1N NaOH/HCl. For measuring concentration dependence of malCEST contrast, phantoms with 2, 4, 6, 8, and 10 mM concentrations of maltitol were prepared in PBS at pH 7.

Phantom imaging. High-resolution ^{1}H NMR phantom experiments from 200 mM maltitol solution were performed on a vertical bore Bruker Avance DMX 400 MHz spectrometer (Bruker Corporation, Germany), equipped with a 5 mm PABBI proton probe using a single pulse experiment with parameters: TR = 4 s, number of averages = 128. ^{1}H MR spectra were gathered at different temperatures (5, 15, 25, 37 °C). A narrow coaxial capillary containing D_2O and TSP was used for locking and chemical shift reference, respectively.

Imaging was performed on a 9.4 T, 30 cm horizontal bore animal MRI scanner (Agilent, USA) interfaced to a Varian console, with a 20 mm volume coil (M2M Imaging, USA). A custom-written segmented spoiled GRE pulse sequence with a frequency selective continuous wave saturation preparation pulse was used to perform CEST experiments. The sequence parameters were: field of view (FOV) = 20 × 20 mm^2, slice thickness = 10 mm, flip angle = 15°, TR = 6.2 ms, TE = 2.9 ms, matrix size = 128 × 128. For every 15 s, one saturation pulse was applied. CEST images were collected using variable saturation lengths (1 through 3 seconds) and saturation pulse amplitudes (B_{1rms}: 2 to 12 μT). For concentration and pH dependent studies, CEST images were collected using 1 second saturation pulse at B_{1rms} of 7 μT for multiple frequencies (−3.4 to +3.4 ppm in 0.2 ppm steps) from bulk water. B_1 and B_0 field maps were also gathered and used to correct the CEST contrast maps. Briefly, CEST data, acquired in the neighborhood of ±1 ppm and WASSR maps were used to generate corrected malCEST images (±1 ppm) using a procedure similar to that described previously[41,52].

Relative B_1 maps were obtained using a magnetization prepared spoiled GRE method. For B_1 correction, two images were obtained using preparation square pulses with duration (τ) and flip angles of 30° and 60°. The RF pulse amplitude for a 30° flip angle was used as the reference B_1 or B_{1ref}. Flip angle (θ) maps were generated by solving the equation:

$$\frac{\cos(2\phi)}{\cos(\phi)} = \frac{S(2\phi)}{S(\phi)}$$

where S(ø) and S(2ø) denote pixel signals in an image with preparation flip angle ø and 2ø respectively. From the flip angle map, a B_1 field map can be obtained using the relation, $B_1 = ø*(360\tau)^{-1}$. The coefficient B_1/B_{1ref} was used for B_1 correction of the malCEST contrast at 1 ppm.

Rat tumor model preparation. The Institutional Animal Care and Use Committees (IACUC) of the University of Pennsylvania approved experimental protocols, and all experiments were carried out in accordance with approved IACUC guidelines.

To validate the malCEST *in vivo*, a rat brain tumor model was used. To develop intracranial tumors, 9 L gliosarcoma cells were used. Syngeneic female Fisher rats (F344/NCR, four-six weeks old) weighing 130–150 grams were used to generate tumor-bearing rats as described previously[41,53]. General anesthesia was induced using 2% isoflurane mixed with 1 liter/min oxygen. A 10 μl suspension of 50,000 9L cells in phosphate buffered saline was injected into the cortex at a depth of 3 mm with a Hamilton syringe and a 30-gauge needle using stereotactic apparatus (3 mm lateral and 3 mm posterior to the bregma). Five weeks after implantation of tumor cells rats were subjected to MRI.

Rat MR imaging. A total of 11 rats were used for imaging. Eight rats were administered with 9 L glioma cells for CEST studies following normal saline (NS, n = 3) and maltitol administration (n = 5). While the remaining 3 rats were used as healthy controls for CEST studies following maltitol administration.

Rats were anesthetized with isoflurane (3% for induction, 1.5% maintenance) and a polyethylene catheter (PE50) was inserted into the tail vein for maltitol or NS injection. MRI imaging was performed on tumor bearing rats five weeks after 9 L cell implantation. Rats were transferred to a 9.4 T horizontal bore small animal MR scanner (Varian, Palo Alto, CA) and placed in a 35 mm diameter commercial quadrature proton coil (m2m Imaging Corp., Cleveland, OH). Animals were kept under anesthesia (1.5% isoflurane in 1 liter/min oxygen) and their body temperature maintained with the air generated and blowing through a heater (SA Instruments, Inc., Stony Brook, NY). Respiration and body temperature were continuously monitored using an MRI compatible small animal monitoring system (SA Instruments, Inc., Stony Brook, NY).

CEST imaging of normal rat brain and rat brain tumors was performed using a similar pulse sequence and parameters as described in the case of phantom imaging except a FOV = 35 × 35 mm^2, slice thickness = 3 mm, matrix size = 128 × 128, B_1 = 2.35 μT, saturation length = 2 s and TR = 8 s. CEST images were collected at multiple frequencies (−3.4 to + 3.4 ppm in 0.2 ppm steps) from bulk water. After baseline imaging the rats were injected maltitol solution at bolus variable rate[54] through the catheter inserted in a tail vein for a period of 60 minutes. Animals received a 300 μl bolus of 1 M maltitol (per 200 gm body weight) intravenously. The rate of the infusion was decreased manually every 1 min followed a decreasing exponential function during the first 8 min and was constant for the remainder of the experiment. The total volume infused was ~1.5 ml. CEST acquisitions were started immediately with the beginning of infusion and acquired at 30-min time interval for a total period of 120 minutes. After CEST imaging, gadolinium-diethylenetriamine pentaacetic acid (Gd-DTPA) (0.3 mmol/kg) was injected through tail vein and T1-weighted imaging was performed on the same anatomical slice used for CEST with GRE (gradient echo) sequence using following parameters: FOV = 35 × 35 mm^2, Flip Angle = 8°, Slice thickness = 3 mm, matrix size = 128 × 128, TR = 6.2 ms, TE = 2.8 ms, and averages = 12.

Similar CEST imaging protocol was used following infusion of NS in glioma bearing rats. Blood glucose and pH measurement at 20, 40 and 60 minutes was also performed using a blood gas analyzer following the administration of maltitol in normal rats.

Image processing. For each pixel in the CEST-weighted images, the z-spectrum was fit to a quadratic polynomial and shifted by the corresponding B_0 offset. B_0 corrected CEST-weighted images are obtained by evaluating the fit at ±1 ppm (S_{+1ppm} and S_{-1ppm}, respectively), and CEST contrast is given by the MTR asymmetry evaluated by Eq. (1).

$$MTR_{asym}(\%) = 100 \times \left(\frac{S_{-ve} - S_{+ve}}{S_0}\right) \quad (1)$$

where S_0 is image with 20 ppm offset saturation. B_1 inhomogeneity was then corrected linearly by pixel-wise dividing by the relative B_1 map. ROIs were manually drawn on tumor and normal appearing brain regions. All image processing and data analysis were performed using software routines written in MATLAB (R2015b) as described in detail elsewhere[14,55].

Statistics. Statistical analyses were performed using SPSS. A student's t-test was performed to compare the changes in the CEST contrast in the normal appearing brain and tumor ROIs following the administration of maltitol intravenously. The data is presented as mean ± standard error.

References

1. Fass, L. Imaging and cancer: a review. *Mol Oncol* **2**, 115–152, https://doi.org/10.1016/j.molonc.2008.04.001 (2008).
2. Akin, O. *et al.* Advances in oncologic imaging: update on 5 common cancers. *CA Cancer J Clin* **62**, 364–393, https://doi.org/10.3322/caac.21156 (2012).
3. Kanal, E. & Tweedle, M. F. Residual or retained gadolinium: practical implications for radiologists and our patients. *Radiology* **275**, 630–634, https://doi.org/10.1148/radiol.2015150805 (2015).
4. Weissleder, R. Molecular imaging in cancer. *Science* **312**, 1168–1171, https://doi.org/10.1126/science.1125949 (2006).
5. Gambhir, S. S. Molecular imaging of cancer with positron emission tomography. *Nat Rev Cancer* **2**, 683–693, https://doi.org/10.1038/nrc882 (2002).
6. Penuelas, I. *et al.* PET Tracers for Clinical Imaging of Breast Cancer. *J Oncol* **2012**, 710561, https://doi.org/10.1155/2012/710561 (2012).
7. Demetriades, A. K., Almeida, A. C., Bhangoo, R. S. & Barrington, S. F. Applications of positron emission tomography in neuro-oncology: a clinical approach. *Surgeon* **12**, 148–157, https://doi.org/10.1016/j.surge.2013.12.001 (2014).
8. Zhou, Z. & Lu, Z. R. Gadolinium-based contrast agents for magnetic resonance cancer imaging. *Wiley Interdiscip Rev Nanomed Nanobiotechnol* **5**, 1–18, https://doi.org/10.1002/wnan.1198 (2013).
9. Kanda, T. *et al.* Gadolinium-based Contrast Agent Accumulates in the Brain Even in Subjects without Severe Renal Dysfunction: Evaluation of Autopsy Brain Specimens with Inductively Coupled Plasma Mass Spectroscopy. *Radiology* **276**, 228–232, https://doi.org/10.1148/radiol.2015142690 (2015).
10. White, G. W., Gibby, W. A. & Tweedle, M. F. Comparison of Gd(DTPA-BMA) (Omniscan) versus Gd(HP-DO3A) (ProHance) relative to gadolinium retention in human bone tissue by inductively coupled plasma mass spectroscopy. *Invest Radiol* **41**, 272–278, https://doi.org/10.1097/01.rli.0000186569.32408.95 (2006).
11. Vinogradov, E., Sherry, A. D. & Lenkinski, R. E. CEST: from basic principles to applications, challenges and opportunities. *J Magn Reson* **229**, 155–172, https://doi.org/10.1016/j.jmr.2012.11.024 (2013).
12. van Zijl, P. C. & Yadav, N. N. Chemical exchange saturation transfer (CEST): what is in a name and what isn't? *Magn Reson Med* **65**, 927–948, https://doi.org/10.1002/mrm.22761 (2011).
13. Kogan, F., Hariharan, H. & Reddy, R. Chemical Exchange Saturation Transfer (CEST) Imaging: Description of Technique and Potential Clinical Applications. *Curr Radiol Rep* **1**, 102–114, https://doi.org/10.1007/s40134-013-0010-3 (2013).
14. Cai, K. *et al.* Magnetic resonance imaging of glutamate. *Nat Med* **18**, 302–306, https://doi.org/10.1038/nm.2615 (2012).
15. Sherry, A. D. & Woods, M. Chemical exchange saturation transfer contrast agents for magnetic resonance imaging. *Annu Rev Biomed Eng* **10**, 391–411, https://doi.org/10.1146/annurev.bioeng.9.060906.151929 (2008).
16. Haris, M., Cai, K., Singh, A., Hariharan, H. & Reddy, R. *In vivo* mapping of brain myo-inositol. *Neuroimage* **54**, 2079–2085, https://doi.org/10.1016/j.neuroimage.2010.10.017 (2011).
17. Haris, M. *et al.* Exchange rates of creatine kinase metabolites: feasibility of imaging creatine by chemical exchange saturation transfer MRI. *NMR Biomed* **25**, 1305–1309, https://doi.org/10.1002/nbm.2792 (2012).
18. Chan, K. W. *et al.* Natural D-glucose as a biodegradable MRI contrast agent for detecting cancer. *Magn Reson Med* **68**, 1764–1773, https://doi.org/10.1002/mrm.24520 (2012).
19. Li, Y. *et al.* Characterization of tumor vascular permeability using natural dextrans and CEST MRI. *Magn Reson Med* **79**, 1001–1009, https://doi.org/10.1002/mrm.27014 (2018).
20. Xu, X. *et al.* The effect of the mTOR inhibitor rapamycin on glucoCEST signal in a preclinical model of glioblastoma. *Magn Reson Med*, https://doi.org/10.1002/mrm.27683 (2019).
21. Crescenzi, R. *et al. In vivo* measurement of glutamate loss is associated with synapse loss in a mouse model of tauopathy. *Neuroimage* **101**, 185–192, https://doi.org/10.1016/j.neuroimage.2014.06.067 (2014).
22. Haris, M. *et al.* Imaging of glutamate neurotransmitter alterations in Alzheimer's disease. *NMR Biomed* **26**, 386–391, https://doi.org/10.1002/nbm.2875 (2013).
23. Jin, T., Wang, P., Zong, X. & Kim, S. G. MR imaging of the amide-proton transfer effect and the pH-insensitive nuclear overhauser effect at 9.4 T. *Magn Reson Med* **69**, 760–770, https://doi.org/10.1002/mrm.24315 (2013).
24. Hwang, Y. Y., Kim, S. G., Evelhoch, J. L. & Ackerman, J. J. Nonglycolytic acidification of murine radiation-induced fibrosarcoma 1 tumor via 3-O-methyl-D-glucose monitored by 1H, 2H, 13C, and 31P nuclear magnetic resonance spectroscopy. *Cancer Res* **52**, 1259–1266 (1992).
25. Jin, T. *et al.* Chemical exchange-sensitive spin-lock (CESL) MRI of glucose and analogs in brain tumors. *Magn Reson Med* **80**, 488–495, https://doi.org/10.1002/mrm.27183 (2018).
26. Jin, T., Mehrens, H., Wang, P. & Kim, S. G. Chemical exchange-sensitive spin-lock MRI of glucose analog 3-O-methyl-d-glucose in normal and ischemic brain. *J Cereb Blood Flow Metab* **38**, 869–880, https://doi.org/10.1177/0271678X17707419 (2018).
27. Nasrallah, F. A., Pagès, G., Kuchel, P. W., Golay, X. & Chuang, K. H. Imaging brain deoxyglucose uptake and metabolism by glucoCEST MRI. *J Cereb Blood Flow Metab* **33**, 1270–1278, https://doi.org/10.1038/jcbfm.2013.79 (2013).
28. Rivlin, M., Tsarfaty, I. & Navon, G. Functional molecular imaging of tumors by chemical exchange saturation transfer MRI of 3-O-Methyl-D-glucose. *Magn Reson Med* **72**, 1375–1380, https://doi.org/10.1002/mrm.25467 (2014).
29. Rivlin, M. & Navon, G. 3-O-Methyl-D-glucose mutarotation and proton exchange rates assessed by. *J Biomol NMR* **72**, 93–103, https://doi.org/10.1007/s10858-018-0209-y (2018).
30. Rivlin, M. & Navon, G. CEST MRI of 3-O-methyl-D-glucose on different breast cancer models. *Magn Reson Med* **79**, 1061–1069, https://doi.org/10.1002/mrm.26752 (2018).
31. Walker-Samuel, S. *et al. In vivo* imaging of glucose uptake and metabolism in tumors. *Nat Med* **19**, 1067–1072, https://doi.org/10.1038/nm.3252 (2013).
32. Xu, Y. Z. & Krnjevic, K. Unlike 2-deoxy-D-glucose, 3-O-methyl-D-glucose does not induce long-term potentiation in rat hippocampal slices. *Brain Res* **895**, 250–252 (2001).
33. Xu, X. *et al.* Dynamic glucose enhanced (DGE) MRI for combined imaging of blood-brain barrier break down and increased blood volume in brain cancer. *Magn Reson Med* **74**, 1556–1563, https://doi.org/10.1002/mrm.25995 (2015).
34. Yadav, N. N. *et al.* Natural D-glucose as a biodegradable MRI relaxation agent. *Magn Reson Med* **72**, 823–828, https://doi.org/10.1002/mrm.25329 (2014).

35. Rivlin, M., Horev, J., Tsarfaty, I. & Navon, G. Molecular imaging of tumors and metastases using chemical exchange saturation transfer (CEST) MRI. *Scientific reports* **3**, 3045, https://doi.org/10.1038/srep03045 (2013).
36. Rivlin, M. & Navon, G. Glucosamine and N-acetyl glucosamine as new CEST MRI agents for molecular imaging of tumors. *Sci Rep* **6**, 32648, https://doi.org/10.1038/srep32648 (2016).
37. Wang, J. *et al*. Magnetic Resonance Imaging of Glucose Uptake and Metabolism in Patients with Head and Neck Cancer. *Sci Rep* **6**, 30618, https://doi.org/10.1038/srep30618 (2016).
38. Longo, D. L. *et al*. *In Vivo* Imaging of Tumor Metabolism and Acidosis by Combining PET and MRI-CEST pH Imaging. *Cancer Res* **76**, 6463–6470, https://doi.org/10.1158/0008-5472.CAN-16-0825 (2016).
39. Schuenke, P. *et al*. Adiabatically prepared spin-lock approach for T1ρ-based dynamic glucose enhanced MRI at ultrahigh fields. *Magn Reson Med* **78**, 215–225, https://doi.org/10.1002/mrm.26370 (2017).
40. Schuenke, P. *et al*. Fast and Quantitative T1ρ-weighted Dynamic Glucose Enhanced MRI. *Sci Rep* **7**, 42093, https://doi.org/10.1038/srep42093 (2017).
41. Bagga, P. *et al*. Non-caloric sweetener provides magnetic resonance imaging contrast for cancer detection. *J Transl Med* **15**, 119, https://doi.org/10.1186/s12967-017-1221-9 (2017).
42. Tolomeo, D. *et al*. Chemical exchange saturation transfer MRI shows low cerebral 2-deoxy-D-glucose uptake in a model of Alzheimer's Disease. *Sci Rep* **8**, 9576, https://doi.org/10.1038/s41598-018-27839-7 (2018).
43. WHO/FAO. Summary of Toxicological Data of Certain Food Additives Series 20: 603. Hydrogenated Glucose Syrups (1985).
44. Lian-Loh, R., Birch, G. G. & Coates, M. E. The metabolism of maltitol in the rat. *Br J Nutr* **48**, 477–481 (1982).
45. Weser, E. & Sleisenger, M. H. Metabolism of circulating disaccharides in man and the rat. *J Clin Invest* **46**, 499–505, https://doi.org/10.1172/JCI105552 (1967).
46. Randtke, E. A., Pagel, M. D. & Cárdenas-Rodríguez, J. QUESPOWR MRI: QUantification of Exchange as a function of Saturation Power On the Water Resonance. *J Magn Reson* **270**, 56–70, https://doi.org/10.1016/j.jmr.2016.06.022 (2016).
47. Sun, P. Z. Simultaneous determination of labile proton concentration and exchange rate utilizing optimal RF power: Radio frequency power (RFP) dependence of chemical exchange saturation transfer (CEST) MRI. *J Magn Reson* **202**, 155–161, https://doi.org/10.1016/j.jmr.2009.10.012 (2010).
48. Sun, P. Z. Simplified quantification of labile proton concentration-weighted chemical exchange rate (k(ws)) with RF saturation time dependent ratiometric analysis (QUESTRA): normalization of relaxation and RF irradiation spillover effects for improved quantitative chemical exchange saturation transfer (CEST) MRI. *Magn Reson Med* **67**, 936–942, https://doi.org/10.1002/mrm.23068 (2012).
49. Sun, P. Z., Wang, Y., Dai, Z., Xiao, G. & Wu, R. Quantitative chemical exchange saturation transfer (qCEST) MRI–RF spillover effect-corrected omega plot for simultaneous determination of labile proton fraction ratio and exchange rate. *Contrast Media Mol Imaging* **9**, 268–275, https://doi.org/10.1002/cmmi.1569 (2014).
50. Zhang, X., Lin, Y. & Gillies, R. J. Tumor pH and its measurement. *J Nucl Med* **51**, 1167–1170, https://doi.org/10.2967/jnumed.109.068981 (2010).
51. Ernst, T., Kreis, R. & Ross, B. D. In *Journal of Magnetic Resonance*, *Series B* Vol. 102, 1–8 (1993).
52. Kim, M., Gillen, J., Landman, B. A., Zhou, J. & van Zijl, P. C. Water saturation shift referencing (WASSR) for chemical exchange saturation transfer (CEST) experiments. *Magnetic resonance in medicine* **61**, 1441–1450, https://doi.org/10.1002/mrm.21873 (2009).
53. Kim, S., Pickup, S., Hsu, O. & Poptani, H. Diffusion tensor MRI in rat models of invasive and well-demarcated brain tumors. *NMR Biomed* **21**, 208–216, https://doi.org/10.1002/nbm.1183 (2008).
54. Fitzpatrick, S. M., Hetherington, H. P., Behar, K. L. & Shulman, R. G. The flux from glucose to glutamate in the rat brain *in vivo* as determined by 1H-observed, 13C-edited NMR spectroscopy. *J Cereb Blood Flow Metab* **10**, 170–179, https://doi.org/10.1038/jcbfm.1990.32 (1990).
55. Haris, M. *et al*. *In vivo* magnetic resonance imaging of tumor protease activity. *Sci Rep* **4**, 6081, https://doi.org/10.1038/srep06081 (2014).

Acknowledgements

We thank Dr. Damodara Reddy for help with Animal Model preparation, Kevin D'Aquilla for help with phantom preparation, and Drs. Stephen Pickup and Weixia Liu for their technical assistance in using the 9.4T horizontal bore animal MR scanner. This work was supported by the NIBIB under Grant No. P41 EB015893 and a grant from Sidra Medical and Research Center.

Author Contributions

P.B. and M.H. contributed to conception and design of the study, performed experiments, analyzed data and wrote the manuscript. N.W., L.R., F.M. and M.D.S. contributed to manuscript writing and editing, H.H. provided the technical support and helped with manuscript editing. R.R. provided conception and overall experimental design and contributed to manuscript writing and editing.

Additional Information

Supplementary information accompanies this paper at https://doi.org/10.1038/s41598-019-47275-5.

Competing Interests: The authors declare no competing interests.

Publisher's note: Springer Nature remains neutral with regard to jurisdictional claims in published maps and institutional affiliations.